nature communications

Article

https://doi.org/10.1038/s41467-025-55854-6

Termination-acidity tailoring of molybdenum carbides for alkaline hydrogen evolution reaction

Received: 31 January 2024

Accepted: 31 December 2024

Published online: 06 January 2025

Check for updates

Zhigang Chen[1,2,6], Minghao Yang[1,2,6], Yifan Li[2,6], Wenbin Gong[3,6], Juan Wang[4], Tong Liu[2], Chunyu Zhang[2], Shuang Hou[2], Guang Yang[2], Hao Li[2], Ye Jin[5], Chunyan Zhang[1], Zhongqing Tian[1], Fancheng Meng[1] & Yi Cui[2]

Transition-metal carbides have been advocated as the promising alternatives to noble-metal platinum-based catalysts in electrocatalytic hydrogen evolution reaction over half a century. However, the effectiveness of transition-metal carbides catalyzing hydrogen evolution in high-pH electrolyte is severely compromised due to the lowered proton activity and intractable alkaline-leaching issue of transition-metal centers. Herein, on the basis of validation of molybdenum-carbide model-catalyst system by taking advantage of surface science techniques, Mo_2C micro-size spheres terminated by Al^{3+} doped MoO_2 layer exhibit a notable performance of alkaline hydrogen evolution with a near-zero onset-potential, a low overpotential (40 mV) at a typical current density of 10 mA/cm^2, and a small Tafel slope (45 mV/dec), as well as a long-term stability for continuous hydrogen production over 200 h. Advanced morphology and spectroscopy characterizations demonstrate that the local -Al-OH-Mo- structures within Al-MoO_2 terminations serve as strong Brønsted acid sites that accelerate the deprotonation kinetics in alkaline HER process. Our work paves an interesting termination-acidity-tailoring strategy to explore cost-effective catalysts towards water electrolysis and beyond.

Sustainable hydrogen energy carrier has emerged as a very promising alternative to current hydrocarbon economy for satisfying the global mission of carbon neutrality[1]. Alkaline hydrogen evolution reaction (HER) presents a feasible and economic pathway to convert intermittent electrical power (e.g., water, solar, and wind) into the green hydrogen molecules at industrial level[2,3]. However, HER process is largely pH-dependent, and kinetically unfavorable in alkaline electrolytes due to the lowered proton activity, and the lack of highly-active protons usually leads to the alkaline HER activity two or three orders of magnitude lower than that in acids[4–6]. Therefore, the exploration of low-cost but highly-efficient HER catalysts holds both fundamental and practical significance in alkaline water electrolysis for large-scale hydrogen production.

Transition-metal carbides (e.g., Mo and W) have been advocated as the most promising candidates to replace benchmark platinum (Pt) catalyst in HER process over half a century because the interstitial carbon atoms of metal carbides affording the metals with similar d-band electronic structure to Pt near the Fermi level[7], consequently, the metal-H strength becomes comparable to that of noble Pt–H bond in associated with the most active protons for HER process[8]. Among various transition-metal carbides catalyzing HER in alkaline mediums, molybdenum carbides have particularly garnered attention due to the

[1]School of Materials Science and Engineering, Chongqing University of Technology, Chongqing, China. [2]i-lab, Vacuum Interconnected Nanotech Workstation (Nano-X), Suzhou Institute of Nano-Tech and Nano-Bionics, Chinese Academy of Sciences, Suzhou, China. [3]School of Physics and Energy, Xuzhou University of Technology, Xuzhou, China. [4]Shanghai Synchrotron Radiation Facility (SSRF), Shanghai Advanced Research Institute, Chinese Academy of Sciences, Shanghai, China. [5]College of Science, Chongqing University of Technology, Chongqing, China. [6]These authors contributed equally: Zhigang Chen, Minghao Yang, Yifan Li, Wenbin Gong. e-mail: ycui2015@sinano.ac.cn

theoretically optimal binding energy of Mo sites and hydrogen intermediates[9,10]. However, their practically alkaline HER activities are still far from the prediction of Pt-like activity due to the lack of comprehensive understanding of the surface chemistry on transition-metal carbides[10–12]. Generally, oxide terminations are inevitably formed on metal carbides during synthesis, storage, and catalysis because of the oxophilicity of transition-metal atoms[13], but the diverse redox chemistry of oxide terminations and their fundamental contributions in catalyzing alkaline HER process are usually negligible and rarely explored. Basically, such oxide terminations are expected to break the HER activity bottleneck of current molybdenum carbides in alkaline mediums, which can be understood from the viewpoint of solid-acid catalyst[14]: (i) the coordinatively unsaturated Mo atoms of low-valence MoO_x termination can function as highly-active Lewis acid sites for the adsorption and activation of water molecules[15], and the underlying carbide structures supply metallic conductivity for the electron transfer process; (ii) the generated protons will spontaneously insert into the MoO_x termination, forming hydrogen molybdenum bronze ($HxMoOy$) species with reversible behaviors of hydrogen adsorption and desorption (also known as Brønsted acid sites)[16,17], which means that the $HxMoOy$ intermediates can serve as a proton sponge to enhance the local proton activity on MoO_x@Mo_2C catalyst surface in high-pH electrolyte, thus fundamentally altering the relatively sluggish kinetics of alkaline HER process into a faster acid-like reaction rate[18]. As recently inferred by several pioneering works including both theoretical prediction and experimental observation, which simultaneously demonstrate that the inherently notable HER activity of molybdenum carbides can indeed be triggered by the surface oxide terminations[19,20]. Unfortunately, such a basic chemistry theory is only confined to acidic mediums, because the oxide terminations with acidic behavior undergo rapid alkaline leaching under high-pH conditions ($MoO_x+OH^- \rightarrow MoO_4^{2-}+H_2O$)[21,22]. This intractable high-pH dissolution issue of oxide terminations generally compromises the theory-predicted Pt-like HER activity for all transition-metal carbides in practical applications[11,13,23]. Therefore, the poor alkaline-leaching resistance of oxide termination might have become the major bottleneck of low-cost molybdenum carbides replacing noble Pt catalyst for highly-efficient HER process under high-pH conditions.

A cation pining effect may provide an interesting route to stabilize the oxide terminations of molybdenum carbides in alkaline electrolyte. Battery materials also undergo composition disintegration and/or dissolution into the electrolytes due to the large lattice variations after long-term electrochemical cycles, where doping an appropriate proportion of solute atoms can be functionally used as pinning points to stabilize the local chemical and electronic structures of host electrode materials[24]. In particular, Al^{3+} atoms have been proven to be very effective for the stabilization of oxide battery materials[25], because the small ionic radius (0.53 Å) of Al^{3+} dopants can effectively avoid physical expansion of the host lattices[26], and meantime the strong host-guest interactions can be achieved by the unusual three positive charges of Al^{3+} centers[27]. Inspired by above thoughts, we believe that the introduction of Al^{3+} atoms can afford the oxide-termination-itself with improved structural robustness. More importantly, Al^{3+} atoms are particularly proficient in tailoring the acidity of molybdenum-oxide terminations by giving rise to abundant bridging hydroxyl species (-Al-OH-Mo-) as strong Brønsted acid sites (proton accumulation and release)[28,29]. These solid-acid sites create an acid-like environment on the oxide-termination catalyst surface in alkaline electrolyte, which not only inhibits the alkaline-leaching behavior of aggressive hydroxyl species from water activation and electrolyte[30], but also enhances the local proton activity for hydrogen production. Given these promising characteristics, exploring the feasibility of introducing Al^{3+} atoms into the oxide termination of molybdenum carbides becomes particularly intriguing for highly active and stable HER process in alkaline electrolyte.

As a powerful surface science approach, model-catalyst system connecting the two worlds of theory and practical catalysis can be used to rapidly pre-investigate the possibility of our hypothesis[31], because the complicated surface chemistries of practical catalyst in liquid electrolytes are usually far from the scope of theory simulations. In our hypothesis, the Al^{3+} modified oxide terminations are potentially beneficial for the activity and stability enhancements of molybdenum carbides catalyzing alkaline HER process. Accordingly, by taking advantage of advanced surface science techniques under high-vacuum conditions, a series of deliberately customized molybdenum-carbide model-catalyst systems can be built up, where the complicated catalyst structures and activity evaluations can be totally simplified for a direct understanding of the relationship between the carbide structure and alkaline HER activity. This will guide the rational design of practical molybdenum-carbide catalysts in the field of alkaline HER electrocatalysis.

Herein, on the basis of validation of molybdenum-carbide model-catalyst system by taking advantage of surface science techniques, we report a feasible carbonization method to synthesize practical Mo_2C nanomaterials with homogeneously distributed Al^{3+} atoms over the amorphous MoO_2 termination (Al-MoO_2@Mo_2C). Comprehensive morphology/spectroscopy/DFT characterizations demonstrate that the unsaturated penta-coordination Al (Al_P) atoms mainly contribute to the acidity tailoring and stabilization of amorphous MoO_2 termination in alkaline electrolyte and the underlying metal-carbide structures supply metallic conductivity for the electron transfer process. Accordingly, the Al_P-MoO_2@Mo_2C cathode exhibits notable HER activities with a near-zero onset-potential and a low overpotential at a typical current density of 10 mA/cm^2 (η_{10} = 40 mV), as well as a small Tafel slope (45 mV/dec), largely excelling most previously reported transition metal carbides and other state-of-the-art catalysts. Moreover, the well-designed Al_P-MoO_2@Mo_2C catalyst also demonstrates a notable stability working at the current density of 10 mA/cm^2, with a negligible activity degradation for continuous hydrogen production over 200 h, showing the practical value of basic model-catalyst system motivating highly-efficient catalyst design towards the replacement of benchmark Pt catalyst in alkaline HER electrocatalysis and beyond.

Results

Model-catalyst system investigates the possibility of our hypothesis

Advanced surface science techniques were performed to build up and evaluate a specific Al-MoO_2@Mo_2C model-catalyst system for investigating the possibility of our hypothesis[31]. In model-catalyst system, a deliberately customized model-catalyst surface can be built up for a direct understanding of the relationship between the catalyst structure and catalytic activity[32]. Accordingly, all model catalysts, including phase-pure Mo_2C (extremely clean metal-carbide surface without any oxide termination), MoO_2@Mo_2C (oxide termination), and Al-MoO_2@Mo_2C (Al^{3+} modified oxide termination), were grown on commercial Mo plates in the near-ambient pressure XPS (NAP-XPS) chamber under controlled temperature and atmosphere conditions. Al-MoO_2@Mo_2C model catalyst was prepared by the carbonization and subsequent oxidation processes of Al^{3+}-adsorbed pretreated Mo plate, as schematically illustrated in Fig. 1a (more synthesis details seen in the method section). All 3D view images of element mapping for above model catalysts are examined by time-of-flight secondary ion mass spectroscopy (TOF-SIMS) technique (Fig. 1b), demonstrating that different types of customized model-catalyst surfaces are indeed obtained. Note that the undesired Na^+ cations of $NaAlO_2$ source have been removed from the metal-carbide product during the carbonization process (Supplementary Fig. 1). The alkaline HER activities of the as-prepared model catalysts were strictly evaluated in a man-made electrochemical cell in glove-box (Fig. 1c), where only the desired model-catalyst surface could contact the alkaline electrolyte for

https://doi.org/10.1038/s41467-025-55854-6

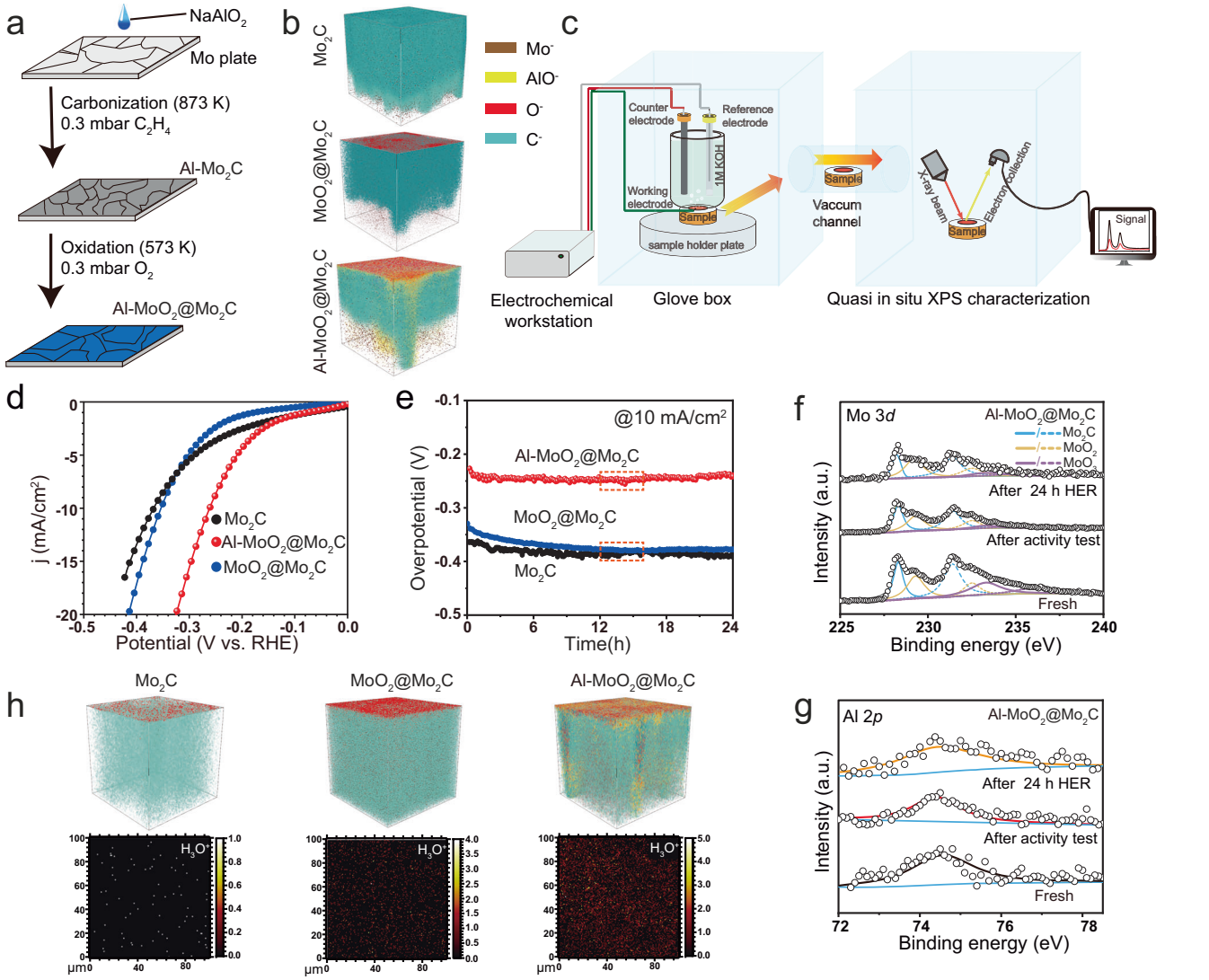

Fig. 1 | Al-MoO_2@Mo_2C model catalyst for alkaline HER process. a The schematic illustration of the preparation of Al-MoO_2@Mo_2C model catalyst in the NAP-XPS chamber. **b** 3D view images of TOF-SIMS element mapping for phase-pure Mo_2C, MoO_2@Mo_2C, and Al-MoO_2@Mo_2C model catalysts. **c** Vacuum-connected glove-box (man-made electrochemical cell) and NAP-XPS system, where the electrochemically treated model catalysts can be transferred to the analysis chamber for XPS measurement through vacuum channel. **d** Polarization (LSV) curves and **e** chronopotentiometry measurements of phase-pure Mo_2C, MoO_2@Mo_2C, and Al-MoO_2@Mo_2C model catalysts. **f** Mo 3*d* and **g** Al 2*p* XPS spectra of fresh and used (after activity test and after long-term hydrogen production) Al-MoO_2@Mo_2C model catalysts. **h** 3D (up) and 2D H_3O^+ (down) view images of TOF-SIMS element mappings for all long-term used model catalysts.

electrolysis. After electrochemical evaluations, the used samples were transferred to the analysis chamber for X-ray photoelectron spectroscopy (XPS) measurements through the vacuum channel (Fig. 1c). In contrast to the high values of η_{10} on phase-pure Mo_2C (368 mV) and MoO_2@Mo_2C (354 mV) counterparts, the desired Mo_2C film tailored by Al^{3+} modified oxide terminations exhibits an obviously enhanced alkaline HER activity with η_{10} as low as 261 mV (Fig. 1d), besides, other electrochemical evaluations, such as stability, Tafel slope, charge-transfer resistance, and ECSA-normalized activity further confirm the notable catalytic performance on Al-MoO_2@Mo_2C model catalyst (Fig. 1e, Supplementary Figs. 2 and 3), suggesting that the introduction of Al^{3+} atoms is indeed beneficial for the improvement of alkaline HER activity and stability for molybdenum-carbide catalyst. XPS and TOF-SIMS measurements for the used (after activity test and long-term stability test) model catalysts can be used to reveal the changes of chemical and electronic structures on these three types of model catalyst surfaces (Supplementary Fig. 4). Mo 3*d* and Al 2*p* XPS profiles are well retained on the used Al-MoO_2@Mo_2C model catalyst (Fig. 1f, g), however, both phase-pure Mo_2C and MoO_2@Mo_2C counterparts (after hydrogen evolution over 24 h) exhibit deep oxidation signals with increased oxide species on the Mo 3*d* XPS spectra after deconvolution (Supplementary Figs. 5 and 6). For the O 1*s* XPS spectra, typical lattice-oxygen and oxygen-vacancy species are well retained on the used Al-MoO_2@Mo_2C model-catalyst surface (Supplementary Fig. 7), suggesting the rich surface-oxide chemistry. 3D view images of TOF-SIMS element mappings for the long-term used model catalysts evidence the good maintenance of Al, Mo, O, and C atoms within Al-MoO_2@Mo_2C model catalyst, while clearly increased oxygen signals are observed on the used MoO_2@Mo_2C and Mo_2C catalyst surfaces (Fig. 1h, up), indicating the structural robustness of desired Al-MoO_2@Mo_2C model catalyst. In addition, 2D view images of TOF-SIMS element mappings and the corresponding profiles reveal that the concentration of H_3O^+ species (acidic indicator) on desired Al-MoO_2@Mo_2C model-catalyst surface is much higher than those of Mo_2C and MoO_2@Mo_2C counterparts (Fig. 1h (down) and Supplementary Fig. 8), demonstrating the achievement of highly acidic surface on Al-MoO_2@Mo_2C model catalyst (Supplementary Fig. 9). Comprehensive electrochemical and spectroscopy characterizations

of these three-types of molybdenum-carbide model catalysts confirm that the introduction of Al additives can be beneficial for the activity and stability improvements of molybdenum-carbide catalyst in alkaline HER process.

Composition and morphological characterizations of Al_P-MoO_2@Mo_2C materials

Guided by the validation of Al-MoO_2@Mo_2C model-catalyst system, the practical Al_P-MoO_2@Mo_2C nanomaterials were synthesized by the carbonization of Al-doped molybdenum oxides coated with organic compounds, as schematically illustrated in Fig. 2a. Initially, Al-doped molybdenum oxides were prepared by a mild solvothermal method at 180 °C for 12 h (Supplementary Figs. 10 and 11). Subsequently, organic carbon sources were introduced following our previously reported method[33], where the as-prepared Al-doped molybdenum-oxide precursors were treated in a mixture solution of polydopamine (DA, 80 mg), polyethylene oxide-co-polypropylene oxide-co-polyethylene oxide (PEO-PPO-PEO, 40 mg), 2-amino-2-hydroxymethyl-propane-1,3-dio (Tris, 20 mg), and distilled water (100 mL) with continuous stirring over 24 h for the formation of organic-compound coated molybdenum oxides. Finally, the organic-compound coated Al-doped molybdenum oxides underwent carbonization at 720 °C for 2 h under Ar atmosphere, resulting in the formation of Al_P-MoO_2@Mo_2C with an optimized Al content of 0.49 wt% in accordance with the coupled plasma optical emission spectrometry (ICP-OES) analysis. For comparison, the MoO_2@Mo_2C counterpart was also prepared according to the same method without the addition of Al source.

The crystal structure of Al_P-MoO_2@Mo_2C materials was verified by X-ray diffraction (XRD) pattern (Fig. 2b). Both Al_P-MoO_2@Mo_2C and MoO_2@Mo_2C samples exhibit characteristic diffraction peaks at 34.7°, 37.9°, 39.7°, 52.4°, 62.2°, 69.6°, 75.2°, and 76.1°, which can be indexed to (100), (002), (101), (102), (110), (103), (112), (201) facets of hexagonal molybdenum-carbide phase with lattice parameters of $a = 3.01$ Å and $c = 4.73$ Å (JCPDS No. 35-0787). Raman spectra was used to examine the surface chemical states of Mo_2C materials with and without Al modification (Fig. 2c). In addition to the intrinsic D (1381 cm^{-1}) and G (1625 cm^{-1}) bands of excessively pyrolyzed carbon materials, the two types of molybdenum carbides exhibit Raman signals at values of 282, 327, 378, 662, 818, and 992 cm^{-1}, which can be ascribed to the features of MoO_2[34,35], suggesting the existence of amorphous molybdenum-oxide termination on the bulk carbide structure of Mo_2C materials. In addition, the completely crystallized MoO_2 layer terminated Mo_2C carbide structure (c-Al-MoO_2@Mo_2C) was synthesized through slightly increasing the pyrolysis temperature of organic coated Al-MoO_x precursors from 720 to 730 °C. Besides of the predominant Mo_2C materials, the XRD pattern also shows typical diffraction signals of (011) and (010) facets for monoclinic MoO_2 phase (JCPDS No. 78-1069) (Supplementary Fig. 12a), and the typically large lattice distance (0.34 nm) of crystallized MoO_2 termination with clear oxide-carbide interface is also evidenced by the scanning transmission electron microscopy (STEM) technique (Supplementary Fig. 12b–e), moreover, the characteristic Raman signals of crystallized MoO_2 materials are very similar to those of amorphous oxide termination (Supplementary Fig. 12f), suggesting that the amorphous oxide structure in desired Al_P-MoO_2@Mo_2C materials is extremely approaching to that of crystallized MoO_2 phase. Scanning electron microscopy (SEM) images of the as-prepared Al_P-MoO_2@Mo_2C materials reveal a sphere-like morphology with diameters ranging from 1 to 2 μm (Fig. 2d and Supplementary Fig. 13a), where the Mo, Al, C, and O elements are preliminary determined by the corresponding energy dispersive X-ray (EDX) spectroscopy (Supplementary Fig. 13b). Advanced STEM characterization was performed to better identify the inner structures of the micro-size spheres, in particular, identifying the bonding interface of the amorphous oxide termination and bulk carbide structure. The cross-sectional sample of Al_P-MoO_2@Mo_2C prepared by focused ion beam (FIB) technique is depicted in Fig. 2e, and the detailed preparation procedures and illustration are shown in Supplementary Fig. 14 (more details seen in the method section), where the middle micro-size spheres are shielded by upper platinum and carbon depositions, and stabilized by underlying Si substrate (Fig. 2e). As illustrated, the big Al_P-MoO_2@Mo_2C micro-size sphere is composed of numerous small Mo-based nanoparticles (Fig. 2f and Supplementary Fig. 15). STEM-EDX line scan technique was used to identify the chemical composition of such small Mo-based nanoparticles. As can be seen, Mo and O elements are determined to exist in the amorphous edges of Mo_2C nanoparticles (Supplementary Fig. 16a), while the typical Mo signal is sharply vanished in the dark regions between Mo_2C nanoparticles (Supplementary Fig. 16b), indicating the presence of pores distributing over the small Mo_2C nanoparticles. Such small pores may serve as the channels for the electrolyte immersion and gas release, thus improving the mass diffusion kinetics on the inner catalyst surface[36,37]. The high-resolution STEM image shows the distinctly crystallized phases are surrounded by amorphous terminations with the interfaces highlighted by yellow dashed lines. Two types of lattice fringes with typical interplanar distances of 2.6 and 2.3 Å are observed on the well-crystallized regions (Fig. 2g and Supplementary Fig. 15b-d), which can be attributed to the (100) and (101) facets of β-Mo_2C, respectively. The corresponding energy dispersive X-ray spectroscopy of STEM (STEM-EDS) mappings demonstrate the homogeneous distributions of Mo, Al, C, and O atoms over the entire cross-sectional morphology of Al_P-MoO_2@Mo_2C micro-size sphere (Fig. 2h and Supplementary Fig. 17).

Evaluation of alkaline HER electrocatalysis on Al_P-MoO_2@Mo_2C catalyst

The alkaline HER performance of Al_P-MoO_2@Mo_2C micro-size sphere catalyst was evaluated in a Ar-saturated 1.0 M KOH (Supplementary Fig. 18) electrolyte using a standard three-electrode system, along with bare carbon (C), MoO_2@Mo_2C counterpart, and commercial Pt/C catalyst as references (evaluations performed in H_2-saturated alkaline electrolyte were shown in Supplementary Fig. 19). All polarization (LSV) curves were recorded without iR corrections and all potentials measured against the Ag/AgCl electrode were calibrated relative to the reversible hydrogen electrode (RHE) (Supplementary Fig. 20). As can be seen, a negligible alkaline HER activity is shown on bare C materials, whereas MoO_2@Mo_2C catalyst exhibits an improved alkaline HER activity with a low overpotential of 98 ± 2 mV (η_{10}) to reach a desired current density of 10 mA/cm^2 (Fig. 3a and Supplementary Fig. 21), indicating the major contributor of the alkaline HER activity should be originated from Mo-based catalyst rather than the excessive carbon materials. Meanwhile, the collected η_{10} activity of our MoO_2@Mo_2C catalyst aligns well with previously reported values of β-Mo_2C catalysts (Supplementary Fig. 22), suggesting the reliability of our evaluation, and extensive efforts have been devoted to the investigations of practically alkaline HER activity on β-Mo_2C catalysts. Encouragingly, our further optimized Al_P-MoO_2@Mo_2C composite catalyst with 0.49 wt% Al additive exhibits a notbale alkaline HER performance, where the current response sharply increases at ~0 V vs. RHE (onset-potential), and the typical η_{10} value is 40 ± 2.5 mV (Fig. 3a and Supplementary Fig. 23), which can be further lowered to 28 mV after 95% iR correction (Supplementary Fig. 24)[38], largely excelling most metal-carbide-dominant HER catalysts reported to date, and is even comparable to that of commercial Pt/C catalyst (Supplementary Table 1). In addition, although the fresh Al_P-MoO_2@Mo_2C and MoO_2@Mo_2C counterpart show the similar low Brunauer–Emmet–Teller (BET) surface areas (S_{BET}) of 4.22 and 3.69 m^2/g, respectively (Supplementary Fig. 25a, b), but an increased BET value is observed on the used Al_P-MoO_2@Mo_2C catalyst (Supplementary Fig. 25c, d), suggesting the activated Al-MoO_2@Mo_2C catalyst indeed possesses high electrochemically active surface area for alkaline HER process. It is noteworthy that the full activation of Al_P-MoO_2@Mo_2C catalyst is achieved

https://doi.org/10.1038/s41467-025-55854-6

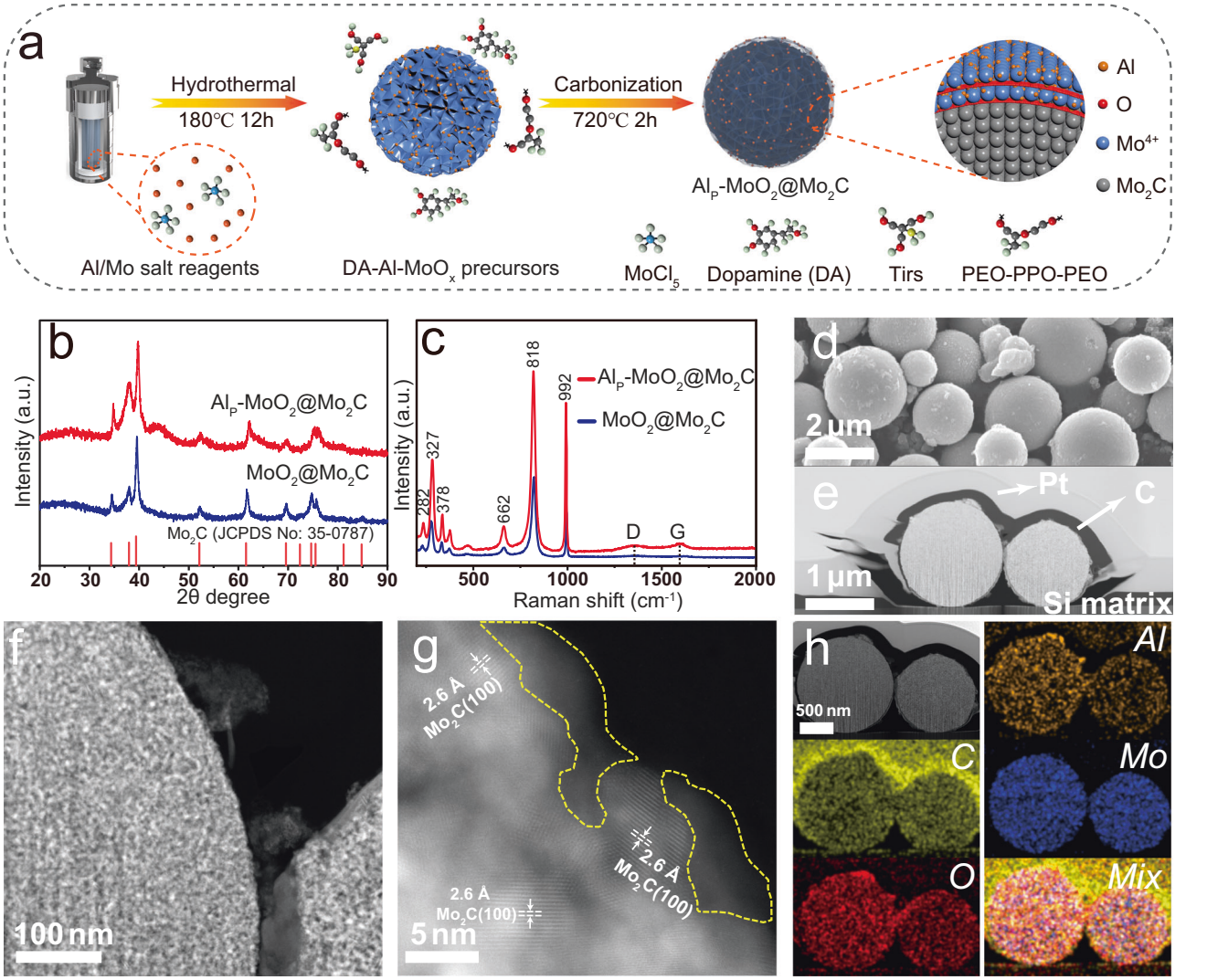

Fig. 2 | Composition and morphology characterizations of Al_P-MoO_2@Mo_2C materials. a Schematic illustration of the synthesis of Al_P-MoO_2@Mo_2C. **b** XRD patterns and **c** Raman spectra of Al_P-MoO_2@Mo_2C and MoO_2@Mo_2C. **d** SEM image of Al_P-MoO_2@Mo_2C micro-size spheres. **e** Cross-sectional TEM image of Al_P-MoO_2@Mo_2C sample, where the upper Pt and C protective layers and underlying Si matrix are marked, respectively. **f** Low-magnification STEM image of an Al_P-MoO_2@Mo_2C micro-size sphere consisting of numerous small nanoparticles. **g** High-magnification STEM image of crystallized Mo_2C and amorphous MoO_2 terminations, with the interfaces highlighted by yellow dashed lines. **h** STEM-EDS mapping of C, O, Al, and Mo elements on the cross-sectional morphology of Al_P-MoO_2@Mo_2C sample (C: yellow, O: red, Al: orange, Mo: blue).

in nearly six scans with a complete overlap of the curves in subsequent scans (Fig. 3b and Supplementary Fig. 26). In contrast, such a self-optimization phenomenon is almost absent on MoO_2@Mo_2C catalyst (Supplementary Fig. 27), suggesting that there is an activation process for Al_P-MoO_2@Mo_2C catalyzing hydrogen production in alkaline electrolyte, and the corresponding inductively coupled plasma mass spectrometer (ICP-MS) characterizations for the post electrolytes evidence the Al-induced activation process on Al_P-MoO_2@Mo_2C catalyst surface during the initial electrolysis (Supplementary Fig. 28). Basically, both the surface inevitable high-valence MoO_3 materials (inert for HER) and supported Al^{3+} species (Al in MoO_3) on Al_P-MoO_2@Mo_2C catalyst are gradually dissolved into the alkaline solutions ($MoO_3 + OH^- \rightarrow MoO_4^{2-} + H_2O$; $Al^{3+} + 4OH^- \rightarrow AlO_2^- + 2H_2O$, where the aggressive OH^- species are mainly from the alkaline electrolyte (open circuit condition) and water dissociation (working condition)), but the dissolution of inert MoO_3 component within Al_P-MoO_2@Mo_2C catalyst is generally lower than that of MoO_2@Mo_2C counterpart without Al modification (the high dissolution concentration of Mo atoms from MoO_2@Mo_2C catalyst surface means the rapid and easy remove of high-valence MoO_3 species), because the unusual three positive charges of Al^{3+} can lead to a strong host-guest interaction between Al center and neighboring MoO_3 component[27], which delays the dissolution of surface MoO_3 component on Al_P-MoO_2@Mo_2C catalyst. In order to further demonstrate the Al-induced slow dissolution of inert MoO_3 component, the dissolved Mo concentrations of Al_P-MoO_2@Mo_2C catalyst after 0 and 6 LSV cycles were detected by ICP-MS technique with MoO_2@Mo_2C as a reference. As expected, the dissolution of inert MoO_3 component within Al_P-MoO_2@Mo_2C catalyst is indeed lower than that of MoO_2@Mo_2C counterpart (Supplementary Fig. 28). When surface inert MoO_3 component of Al_P-MoO_2@Mo_2C catalyst is removed, besides, the coordination environment of Al^{3+} centers are well regulated, the retained Al^{3+} species within active MoO_2 termination on bulk Mo_2C carbide structure can catalyze hydrogen evolution efficiently and stably. The reaction kinetics of alkaline HER process can be extracted from the corresponding Tafel plot, where the smaller Tafel slope usually means the faster reaction rate of hydrogen

https://doi.org/10.1038/s41467-025-55854-6

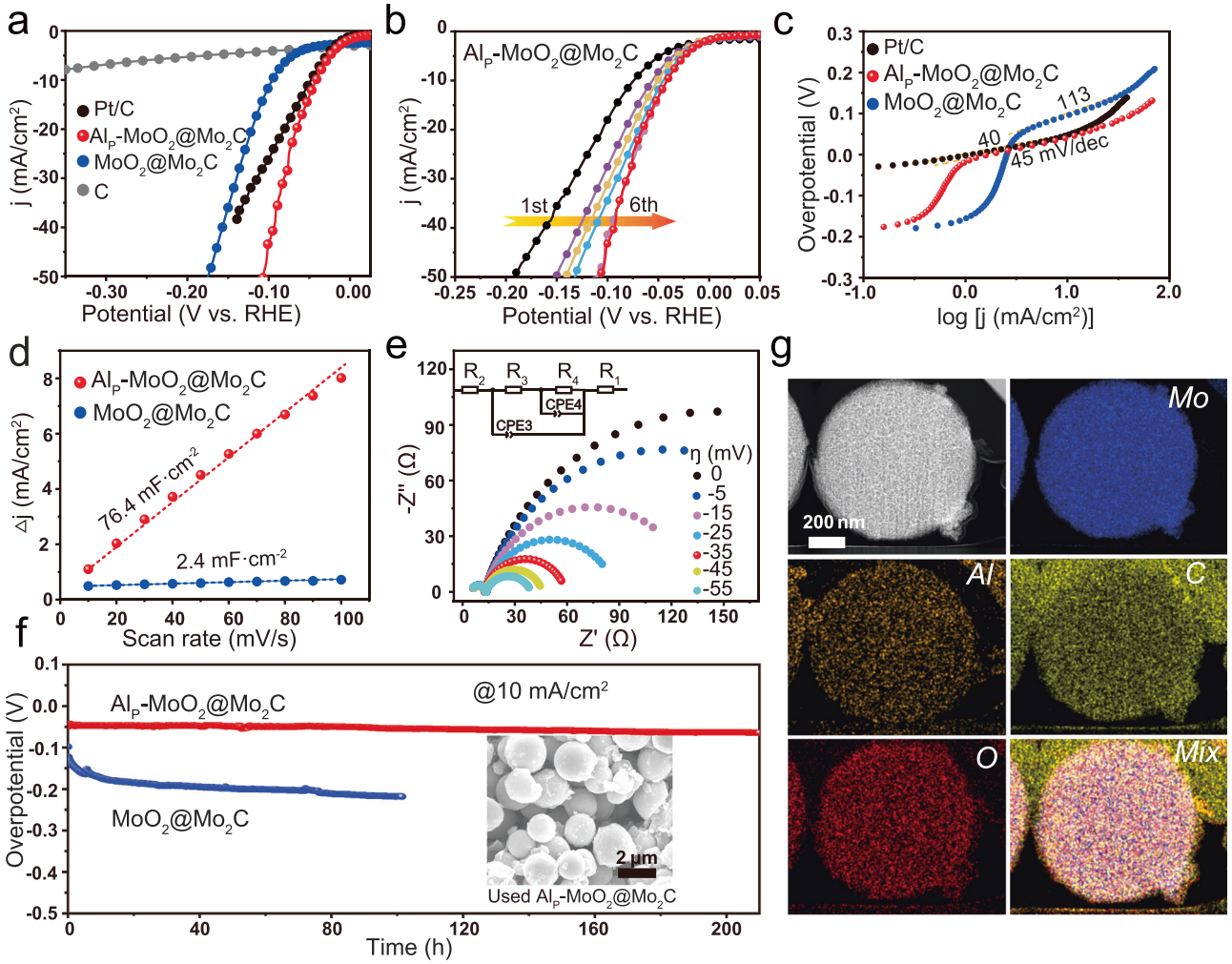

Fig. 3 | The evaluation of HER performance of AlP-MoO2@Mo2C catalyst in 1.0 M KOH electrolyte (pH = 14 ± 0.1, Rs = 3.4 ± 0.3, mass loading = 2.83 mg/cm², room temperature = 298 K). a Polarization (LSV without iR correction) curves of C (gray), $MoO_2@Mo_2C$ (blue), Al_P-$MoO_2@Mo_2C$ (red) and commercial Pt/C (black) catalysts. **b** Six scans of the polarization (LSV) curves illustrating the full activation process for Al_P-$MoO_2@Mo_2C$ catalyst. **c** Tafel plots of $MoO_2@Mo_2C$ (blue), Al_P-$MoO_2@Mo_2C$ (red) and commercial Pt/C (black) catalysts. **d** Determination of C_{dl} values of $MoO_2@Mo_2C$ and Al-$MoO_2@Mo_2C$ catalysts by plotting the current-density variation (Δj) against the scan rates (10–100 mV/s). **e** Potential-dependent Nyquist plots of Al_P-$MoO_2@Mo_2C$ catalyst, with the inset showing the equivalent circuit for the simulation. **f** Chronopotentiometry measurement of Al_P-$MoO_2@Mo_2C$ and $MoO_2@Mo_2C$ catalysts with the SEM image of used Al_P-$MoO_2@Mo_2C$ sample in the insert. **g** STEM-EDS mappings of used Al_P-$MoO_2@Mo_2C$ showing the homogeneous distributions of C (yellow), O (red), Mo (blue) and Al (orange) elements.

production. In contrast to the sluggish kinetics observed in alkaline HER process for the $MoO_2@Mo_2C$ counterpart, our well-designed Al_P-$MoO_2@Mo_2C$ catalyst exhibits a lowered Tafel slope (45 ± 2 mV/dec) (Fig. 3c and Supplementary Fig. 29), which can be further decreased to 42 mV/dec after 95% iR correction (Supplementary Fig. 24c), being very close to the value (40 mV/dec) of benchmark Pt/C catalyst, suggesting a substantial alteration in the chemical environment of adsorbed protons on Al_P-$MoO_2@Mo_2C$ catalyst surface, bringing it in line with the referenced Pt surface[9]. Meanwhile, the reaction kinetics of $MoO_2@Mo_2C$ and Al_P-$MoO_2@Mo_2C$ catalysts are also compared in accordance with the directly measured Tafel plots (Supplementary Fig. 30a)[39]. Notably, Al_P-$MoO_2@Mo_2C$ sample still exhibits a lower cathodic Tafel slope (50 mV/dec) than that of $MoO_2@Mo_2C$ (130 mV/dec) (Supplementary Fig. 30b), suggesting the faster reaction kinetics of HER process on Al_P-$MoO_2@Mo_2C$ catalyst surface. The electrochemical surface area (ECSA) is an effective parameter to demonstrate the Al function in Al_P-$MoO_2@Mo_2C$ catalyst for activating more surface inert atoms in alkaline HER process, which can be revealed by the double-layer capacitance (C_{dl}) through cyclic voltammetry (CV) measurements. The larger C_{dl} usually means more available active sites in electrochemical reaction. The C_{dl} value of Al_P-$MoO_2@Mo_2C$ catalyst is determined to be as high as 76 mF/cm², nearly 31-fold enhancement than that of $MoO_2@Mo_2C$ counterpart (Fig. 3d and Supplementary Fig. 31). The contact angle (hydrophilicity) and temperature-dependent resistivity (conductivity) measurements demonstrate the appealing catalyst surface of Al_P-$MoO_2@Mo_2C$ with desired chemical and electronic structures (Supplementary Fig. 32), thus giving rise to high ECSA value. With more inert atoms activated on Al_P-$MoO_2@Mo_2C$ catalyst surface, the following water dissociation and produced H* intermediates on Al_P-$MoO_2@Mo_2C$ catalyst surface were traced by the potential-dependent electrochemical impedance spectroscopy (EIS) measurements (Fig. 3e)[18]. All collected Nyquist plots exhibit two semicircles with a similar onset-point. After simulated by the equivalent circuit model (inset in Fig. 3e, Supplementary Fig. 33 and Table 2), R_1 is the uncompensated solution resistance (R_s, Supplementary Fig. 34), R_2 suggests the charge transfer resistance from the bulk carbide structure (Mo_2C) to the oxide-termination catalyst surface (Al_P-MoO_2) at high frequencies, which is almost independent on the applied overpotentials, suggesting the intrinsically fast electron transfer behavior of the underlying metal-carbide structures, also evidencing

the structural robustness of bonding interfaces between Mo_2C and Al_P-MoO_2 components[40]. However, R_3 and R_4 are largely depended on the applied overpotentials, where R_3 represents the charge transfer resistance caused by the adsorbed water molecules at low frequencies, while R_4 originates from the proton accumulation caused by produced protons inserting into the amorphous Al-MoO_2 layer (Al-H*x*MoO*y*). Both decrease when increasing the applied overpotentials. In particular, R_3 decreases to 8.5 Ω at applied overpotential of 35 mV, suggesting the fast charge transfer kinetics between Al-MoO_2 termination to the adsorbed H_2O molecules for the cleavage of H−OH bonds. The decreased values of R_4 parameter feature the enrichment of protons on Al-MoO_2 termination through the formation of Al-H*x*MoO*y* intermediates under low overpotentials. In contrast, the MoO_2@Mo_2C counterpart exhibits inferior HER activity, as determined by the potential-dependent EIS plots (Supplementary Fig. 35). In addition, both ECSA-normalized activity and TOF values have also been given to compare the activity of MoO_2@Mo_2C and Al_P-MoO_2@Mo_2C catalysts in accordance with previous reports[41,42]. Although the high C_{dl} value (rich surface Mo and O sites activated by the low-loading Al^{3+} atoms) results in a lowered activity in comparison with that of MoO_2@Mo_2C counterpart after ECSA normalization (Supplementary Fig. 36a), Al_P-MoO_2@Mo_2C catalyst still yields a high TOF value of $0.014 \pm 0.001\ s^{-1}$ at the overpotential of 50 mV, nearly fourfold enhancement than that of MoO_2@Mo_2C counterpart catalyst (Supplementary Fig. 36b, c), demonstrating the activity improvement of MoO_2@Mo_2C by low-loading Al modification. The calculated average Faraday efficiency of the desired Al_P-MoO_2@Mo_2C catalyst is up to 96.6% (96.6% ± 1%) (Supplementary Fig. 37), indicating the high selectivity of hydrogen production.

Another critical concern of a notable electrocatalyst for practical application is the long-term durability performance. As shown in Fig. 3f, in contrast to the gradually increasing overpotentials maintaining the constant current density of 10 mA/cm^2 on MoO_2@Mo_2C counterpart, our well-designed Al_P-MoO_2@Mo_2C catalyst demonstrates a notable stability in catalytic activity over 200 h of continuous hydrogen production at the typical current density of 10 mA/cm^2, excelling most of previously reported molybdenum-carbide catalysts under the same current-density condition (Supplementary Fig. 38). Furthermore morphology characterizations of the used Al_P-MoO_2@Mo_2C catalyst reveal that the micro-size sphere, consisting of carbide structures and Al-MoO_2 terminations, are well retained (Fig. 3f, g, Supplementary Figs. 39–41). Also, ICP-MS detection of the post-electrotes has been performed to evaluate the possible Mo dissolution from Al_P-MoO_2@Mo_2C and MoO_2@Mo_2C catalysts at different catalysis stages. Besides of the inevitable dissolution of high-valence MoO_3 at the initial activation process, no obvious Mo dissolution is detected in the alkaline electrolyte after long-term hydrogen production over 200 h. In contrast, one could notice that the concentration of Mo element is up to 2.0 ppm in less than 10 h for the MoO_2@Mo_2C counterpart (Supplementary Fig. 42). This experiment evidences indicate that the Al^{3+} atoms tailoring strategy can afford the active MoO_2 termination with improved dissolution resistance in alkaline electrolyte. In addition, Mo_2C carbide-structure terminated by completely crystallized MoO_2 layer was synthesized through slightly regulating the synthesis conditions (which will guide the following construction of amorphous MoO_2 termination in calculation section). The synthesized Mo_2C phase with complete MoO_2 termination also shows a considerable long-term catalytic stability with hydrogen production over 24 h (Supplementary Fig. 43a), but its practical alkaline HER activity is inferior than that of Al_P-MoO_2@Mo_2C catalyst (Supplementary Fig. 43b). To this end, we can conclude that the slightly crystallized MoO_2 clusters may be beneficial for the stabilization of inner Mo_2C carbide structure, but cannot improve the alkaline HER activity of Mo_2C phase intrinsically.

Elucidation of the structural robustness of Al_P-MoO_2@Mo_2C materials

Comprehensive spectroscopy characterizations of the used catalyst can yield valuable insights into the improved structural robustness of Al_P-MoO_2@Mo_2C materials in alkaline electrolyte, with the sample soaked solely in electrolyte as the fresh reference. XRD and Raman characterizations rapidly confirm the maintenance of Mo_2C-domain and amorphous MoO_2 termination on the used Al_P-MoO_2@Mo_2C composite catalyst (Supplementary Fig. 44), and the concentration of dissolved Al species in the post-alkaline electrolyte (hydrogen production over 24 h) is rather low (Supplementary Fig. 45), suggesting that the Al_P-MoO_2 termination on Mo_2C carbide structure is less prone to dissolution in alkaline electrolyte. XPS was used to investigate the changes in the bonding configurations of Al_P-MoO_2@Mo_2C composite catalyst after alkaline HER process. Upon deconvolution, all fresh and used samples exhibit three pairs of peaks. The major peaks at low binding energies (228.6 eV for Mo $3d_{5/2}$ and 231.8 eV for Mo $3d_{3/2}$) are associated with the intrinsic Mo-C/Mo-Mo bonds in β-Mo_2C phase, while the second pair of peaks at middle binding energies (229.5 eV for Mo $3d_{5/2}$ and 233.2 eV for Mo $3d_{3/2}$) is assigned to the Mo^{4+} species of amorphous MoO_2 layer. Additionally, peaks of the inevitable high-valence MoO_3 species are observed at higher binding energies (233.3 for Mo $3d_{5/2}$ and 235.9 eV for Mo $3d_{3/2}$). In order to better compare the changes of each component (Mo_2C, MoO_2, MoO_3) for fresh and used catalysts, their contents were determined in accordance with XPS peak areas after deconvolution. As shown in Fig. 4a, Supplementary Fig. 46 and Table 3, both fresh and used Al-MoO_2@Mo_2C catalysts higher contents of Mo_2C component than those of corresponding states of MoO_2@Mo_2C counterparts, besides, more Mo^{6+} species are observed on used MoO_2@Mo_2C counterpart, indicating the structural robustness of Al_P-MoO_2 termination in protecting the bulk carbide structure in alkaline electrolyte. The chemical state of Al species within MoO_2 termination was identified by Al 2*p* XPS spectra (Fig. 4b). In both fresh and used Al_P-MoO_2@Mo_2C catalysts, Al atoms predominantly exist in a triplet valence state, suggesting they are coordinated by oxygen atoms in the oxide termination. However, the used Al_P-MoO_2@Mo_2C sample exhibits a slightly increased binding energy of the Al 2*p* signal relative to the fresh one, implying the aggressive hydroxyl anions may preferentially adsorb on the Al centers (Al^{3+} atoms as active sites), thereby alleviating the accumulation of interfacial OH^- species for the dissolution of neighboring Mo^{4+} acidic sites ($MoO_2 + OH^- \rightarrow MoO_4^{2-} + H_2O$)[30]. The local atomic and electronic structures of Mo atoms in both fresh and used Al_P-MoO_2@Mo_2C samples were further examined by X-ray adsorption spectra (XAS). The positive-shifting white-line peak of Mo K-edge XANES and rather weak Mo-Mo coordination strength (EXAFS R-space) suggest the deep oxidation of the used MoO_2@Mo_2C counterpart[43] (Supplementary Fig. 47). In contrast, the normalized X-ray absorption near-edge structure (XANES) profiles of Mo K-edge reveal that the adsorption positions of fresh and used Al_P-MoO_2@Mo_2C samples are located between commercial Mo_2C and MoO_2 references, and are extremely approaching to that of commercial Mo_2C powder (Fig. 4c). Furthermore, the XANES profiles of fresh and used Al_P-MoO_2@Mo_2C samples resemble that of commercial Mo_2C reference (Fig. 4c), indicating the robust Al-MoO_2 termination benefits the stabilization of bulk carbide structure in alkaline electrolyte. The R-space profiles obtained from Fourier transform extended X-ray absorption fine structure (FT-EXAFS) spectra, combined with the corresponding Wavelet transform EXAFS (WT-EXAFS), reveal that the bulk carbide structure of used Al_P-MoO_2@Mo_2C remains nearly unchanged with negligible enhancement of oxide termination relative to the fresh sample (Fig. 4d, e). This observation strongly suggests the structural robustness of Al_P-MoO_2@Mo_2C composite catalyst. In addition, we also observe that the intensities of metallic Mo-Mo scattering path in both fresh and used Al_P-MoO_2@Mo_2C samples are

https://doi.org/10.1038/s41467-025-55854-6

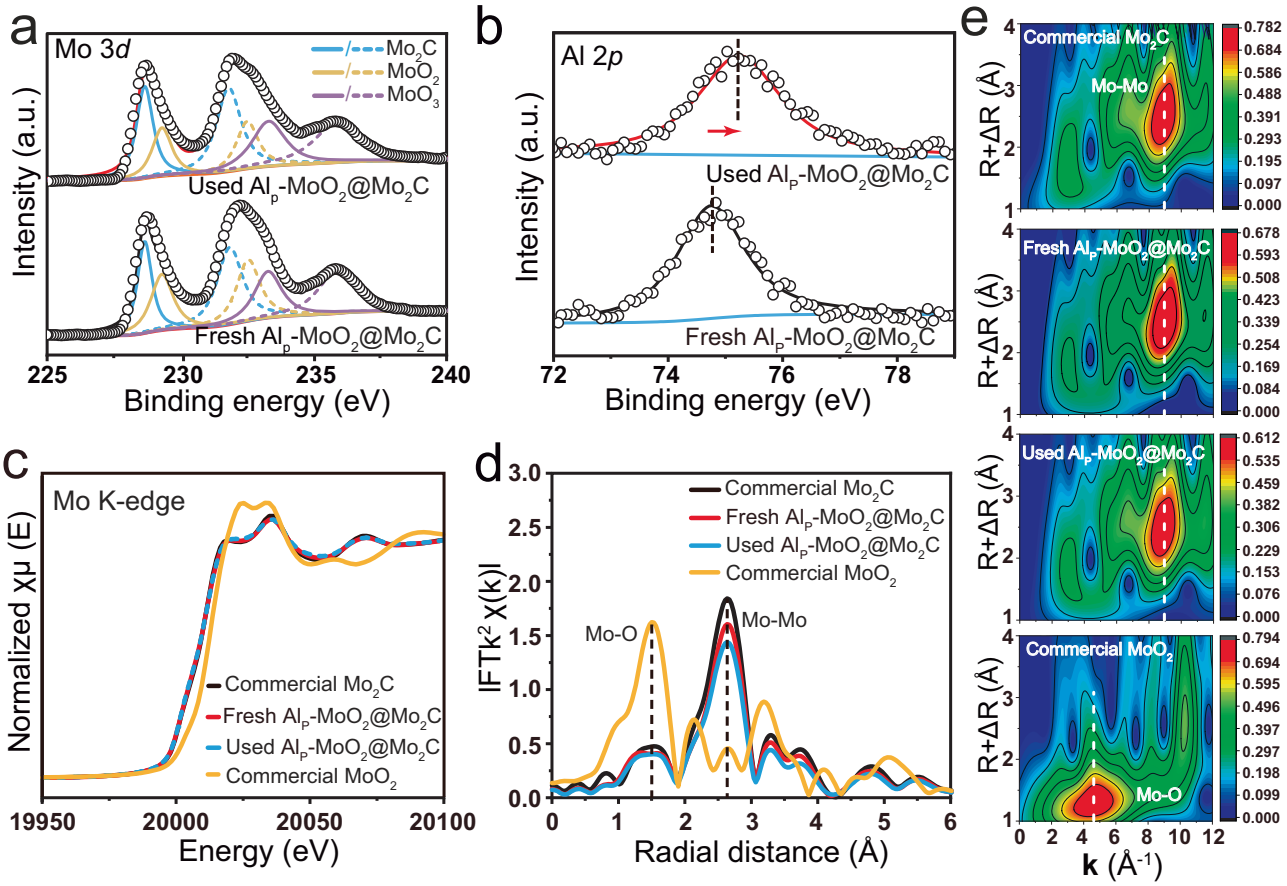

Fig. 4 | The elucidation of the origin of structural robustness of Al-MoO_2@Mo_2C materials. a Mo 3*d* and **b** Al 2*p* XPS spectra of both fresh Al_P-MoO_2@Mo_2C and used Al_P-MoO_2@Mo_2C. **c** Mo K-edge NEXANES spectra of fresh Al_P-MoO_2@Mo_2C and used Al_P-MoO_2@Mo_2C, along with commercial Mo_2C and MoO_2 references. **d** Corresponding R-space profiles from the FT-EXAFS spectra. **e** WT-EXAFS plots, where R and ΔR represent uncorrected distance and phase shift, respectively, and *k* is the wavevector.

slightly weaker than that of commercial Mo_2C powder. This discrepancy arises from the oxidation of partial Mo−Mo metallic bonds in nano-scale Mo_2C materials, leading to the formation of termination on the carbide structure. Based on the aforementioned structural characterizations, we can reasonably conclude that Al^{3+} atoms play a crucial role in stabilizing low-valence oxide termination, thereby preventing the bulk carbide structure from deep oxidation in alkaline electrolyte.

Termination-acidity tailoring of Mo_2C by penta-coordination Al^{3+} sites

The subtle changes in chemical environment on the surface of used Al_P-MoO_2@Mo_2C catalyst were investigated by multiple high-resolution spectroscopy characterizations, which can deepen our understanding of the markedly improved alkaline HER activity of Al_P-MoO_2@Mo_2C catalyst. First, the O 2*p* XPS of used Al_P-MoO_2@Mo_2C catalyst demonstrates a higher abundance of adsorbed hydroxyl and H_2O species compared to the used MoO_2@Mo_2C counterpart (Supplementary Fig. 48), suggesting that Al^{3+} tailoring of MoO_2 termination gives rise to a highly hydrophilic surface. In contrast to the fresh sample, the O K-edge near edge X-ray absorption fine structure (NEXAFS) spectra of used Al_P-MoO_2@Mo_2C catalyst exhibits a markedly increased intensity of Mo 4*d*-O 2*p* (e_g) hybridization at ~540.9 eV, which is much higher than that of used MoO_2@Mo_2C counterpart (Fig. 5a). The increase suggests that partial O 2*p* orbitals of Mo 4*d*-O 2*p* (e_g) hybridization are covalently shared by the produced protons during alkaline HER process, contributing to the formation of H*x*MoO*y* intermediates on Al_P-MoO_2@Mo_2C catalyst surface[44]. Second, the acidic surface formed by H*x*MoO*y* intermediates on used Al_P-MoO_2@Mo_2C catalyst was further detected by TOF-SIMS technique. Compared to the fresh samples, signals of hydrogen-containing species including H_3O^+, Al-OH, and Mo-OH on the used ones clearly increase (Fig. 5b, c, Supplementary Figs. 49 and 50). In particular, the main acid indicator of increased H_3O^+ signal directly indicates the realization of a local acid-like environment on Al_P-MoO_2@Mo_2C catalyst surface in alkaline electrolyte. Third, the chemical properties of H*x*MoO*y* acidic intermediates are further analyzed by solid-state ^1H magic-angle-spinning nuclear magnetic resonance (^1H MAS NMR) spectra. The fresh and used Al_P-MoO_2@Mo_2C samples exhibit two distinct peaks at 1.3 and 4.9 ppm (Fig. 5d and Supplementary Fig. 51), which can be attributed to the terminal (OH_t) and bridging (OH_b) hydroxyl species, respectively[45–47]. A notably enhanced OH_b signal on the used Al_P-MoO_2@Mo_2C catalyst relative to the fresh sample suggests that the bridging oxygen sites are highly effective for the adsorption of produced protons. In addition, the function of Al^{3+} atoms are elucidated by Al K-edge and ^{27}Al NMR spectra. Al K-edge XANES spectra reveals that the predominant octahedral (Al_O) and tetrahedral (Al_T) coordination structures of Al centers are still retained on the used Al_P-MoO_2@Mo_2C sample (Fig. 5e)[48]. More detailed identification of chemical environments of Al centers was examined by ^{27}Al NMR spectra: (i) compared to the fresh sample, the vanished Al_P signal (~35 ppm) of used sample suggests that the unsaturated penta-coordination Al^{3+} atoms serve as the active sites in alkaline HER process (Fig. 5f)[49,50]; (ii) the distinctly split peaks (−0.33, +11.7 ppm) of used

https://doi.org/10.1038/s41467-025-55854-6

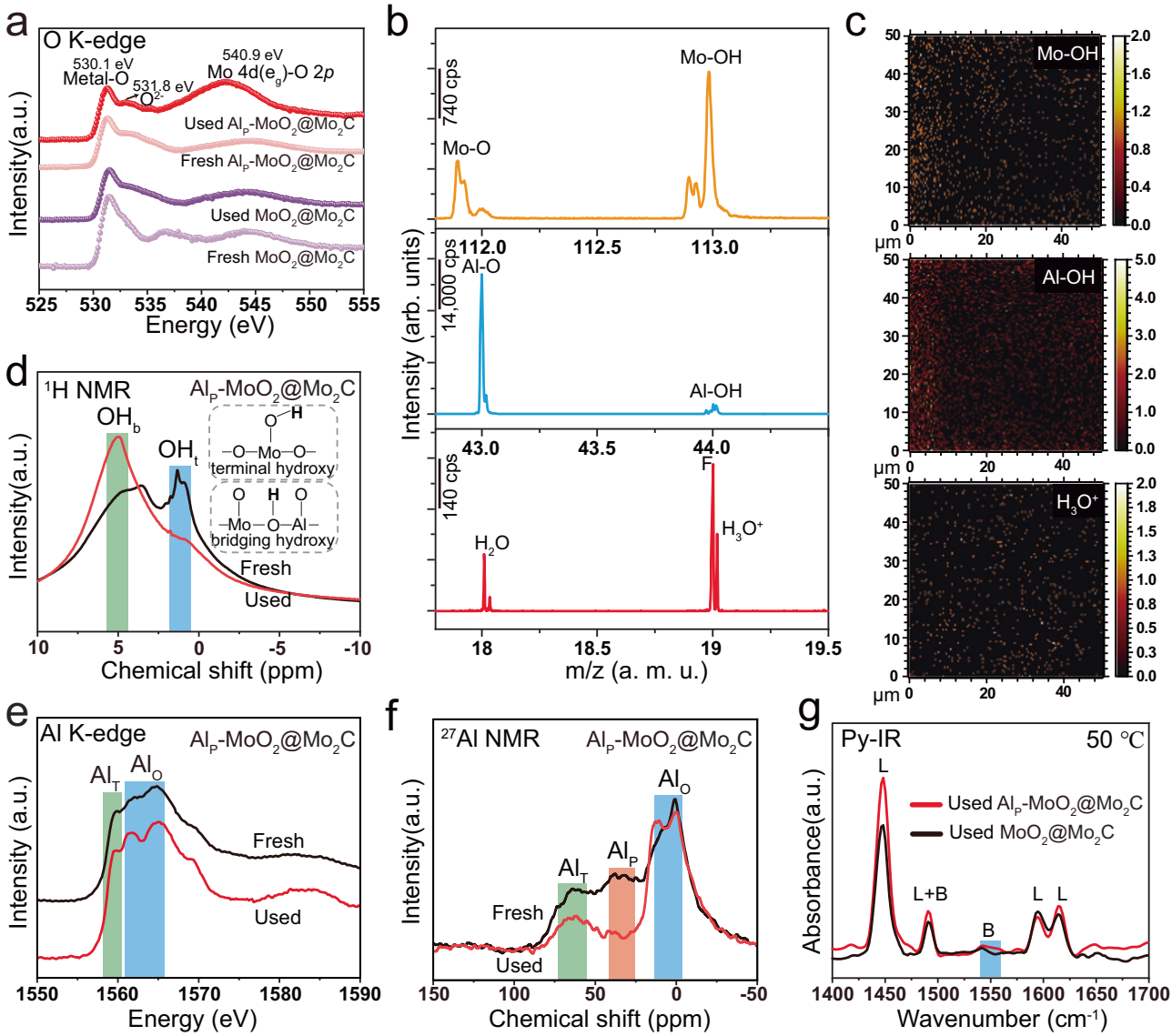

Fig. 5 | Multiple high-resolution spectroscopy characterizations advancing the comprehension of enhanced alkaline HER activity on Al_P-MoO_2@Mo_2C catalyst. a O K-edge NEXAFS spectra of fresh and used Al_P-MoO_2@Mo_2C catalysts. **b** TOF-SIMS profiles of used Al_P-MoO_2@Mo_2C catalyst with signals of H_3O^+, Al-OH, and Mo-OH species, where the fluorine signal (F, $m/z = 19.00$) may originate from the inevitable contamination of fluorine-containing sealing ring in the analysis chamber during Bi^{3+} cations impacting the sample, while the H_3O^+ species can be responsible for the higher signal at m/z = 19.02. **c** 2D distribution images of H_3O^+, Al-OH, and Mo-OH species on used Al_P-MoO_2@Mo_2C catalyst surface. **d** ^{1}H NMR, **e** Al K-edge XANES and **f** ^{27}Al NMR spectra of fresh and used Al_P-MoO_2@Mo_2C samples. **g** Py-IR spectra of used MoO_2@Mo_2C and Al_P-MoO_2@Mo_2C collected at 50 °C.

sample imply that the chemical state of octahedral-coordination Al (Al_O) sites might have been slightly altered due to the adsorption of produced protons (Fig. 5f)[51,52]. By combining the analysis of ^{1}H and ^{27}Al NMR, and Al K-edge XANES spectra, we can speculate that the bridging oxygen atoms in the -Al-O-Mo- structure may serve as ideal adsorption sites for dissociated H* intermediates (Al_P-H*x*MoO*y*) on Al_P-MoO_2@Mo_2C catalyst surface. Finally, the deprotonation kinetics of H*x*MoO*y* intermediates is determined by their acidity, which was examined by pyridine infrared (Py-IR) spectra (Fig. 5g)[53]. The Py-IR spectra of used Al_P-MoO_2@Mo_2C collected at 50 °C shows much stronger Brønsted-acid signals at 1540 and 1640 cm^{-1} when comparing to used MoO_2@Mo_2C counterpart, suggesting that the bridging -Al-OH-Mo- structure can provide more available Brønsted acid sites. Furthermore, the signal at 1542 cm^{-1} corresponding to Brønsted acid sites is still retained on the used Al_P-MoO_2@Mo_2C sample at 150 °C (Supplementary Fig. 52), while it is almost absent on MoO_2@Mo_2C counterpart. This indicates a notable enhancement of the acidity for Al_P-H*x*MoO*y* intermediates[54].

DFT calculations

First-principle density functional theory (DFT) calculations were performed to predict the influence of Al^{3+} tailoring on the chemical and electronic structures of MoO_2 termination on Mo_2C carbide phase. The selections of $(001)_{Mo2C}$ and $(010)_{MoO2}$ facets in DFT models were in accordance with aforementioned experiment evidences and the evaluations of lattice mismatch and interface charge-transfer behavior (Supplementary Fig. 53, Supplementary data 1–3). Detailed different views of all established DFT models (clean surface) are shown in Fig. 6a and Supplementary Fig. 54. Electron localized function (ELF) and Bader charge calculations simultaneously demonstrate the accumulation of more electrons centered at the bridging oxygen atoms between the Mo and Al hetero-nuclear atoms, with the values of charge localization

https://doi.org/10.1038/s41467-025-55854-6

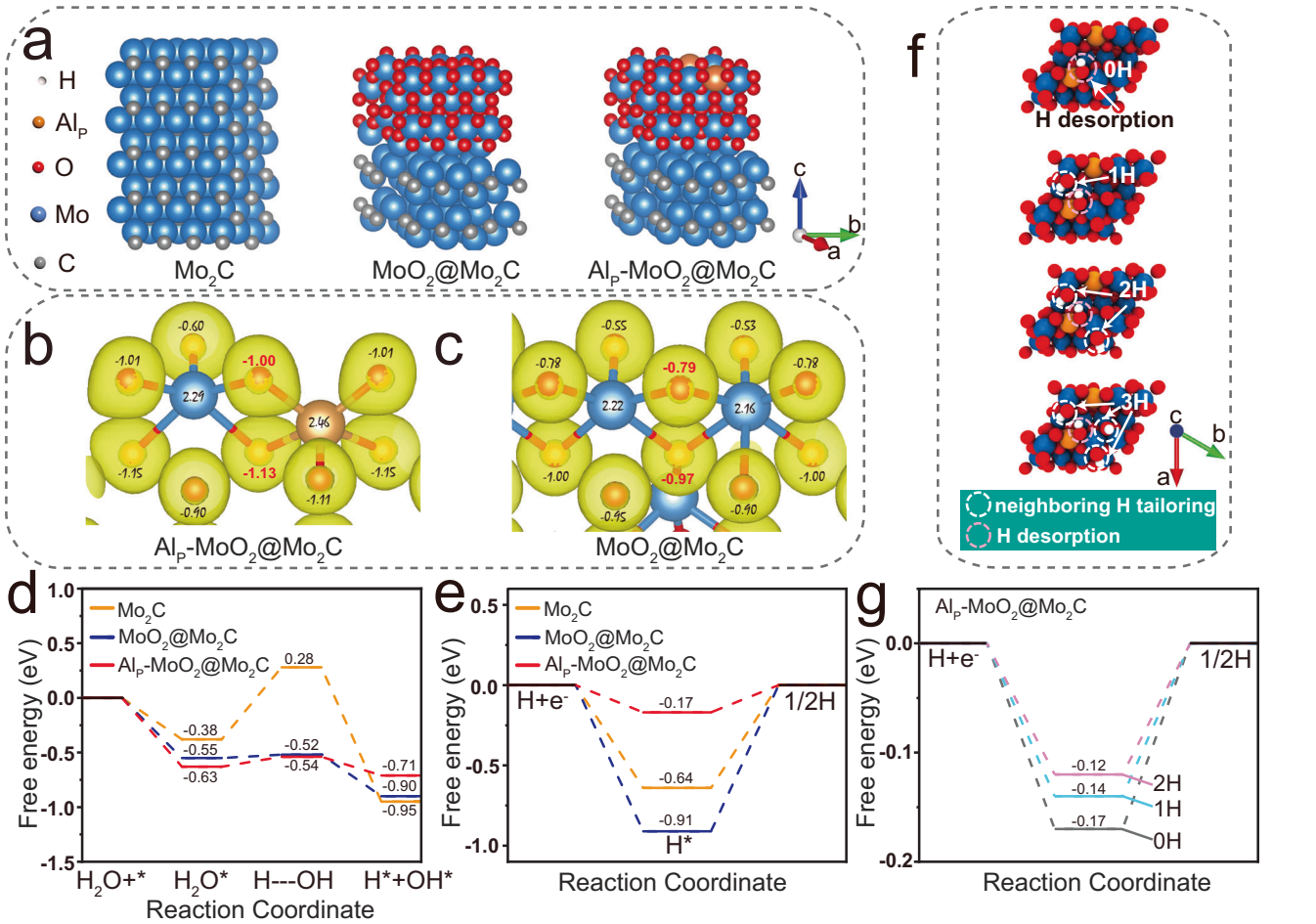

Fig. 6 | DFT calculations for the prediction of alkaline HER activity on Al_P-MoO_2@Mo_2C catalyst model. a The established theoretical models of bare Mo_2C, MoO_2@Mo_2C, and Al_P-MoO_2@Mo_2C. ELF and Bader charge calculations on **b** Al_P-MoO_2@Mo_2C and **c** MoO_2@Mo_2C models, where the yellow bubbles indicate the charge localization. The calculated free energy diagrams for **d** water adsorption and dissociation, and **e** hydrogen desorption step on bare Mo_2C, MoO_2@Mo_2C, and Al_P-MoO_2@Mo_2C models. **f** The schematically illustration of the desired H* atom tuned by neighboring Brønsted acid sites and **g** the corresponding calculated free energy diagrams. Panels **a**, **b**, **c**, and **f** are created by VESTA and VMD software[63,64].

highlighted by red color (Fig. 6b, c), implying that the strong electronegativity oxygen sites within Al-MoO_2@Mo_2C catalyst are energetically favorable for the adsorption of positive H^+ intermediates from water dissociation.

Given the well-designed chemical environment of Al_P-MoO_2@Mo_2C catalyst surface for the adsorption of dominant H^* intermediates in HER process, theoretical evaluations of water dissociation and hydrogen desorption activities were performed. As the solvation effect has no obvious influence on the binding-energy calculations (Supplementary Fig. 55)[55,56], all simulations were performed under the vacuum condition. The whole alkaline HER process consists of the initial state (IS, H_2O*), transition state (TS, H---OH), final state (FS, H* + OH*) (Supplementary data 4–6). The classic Nudged Elastic Band (NEB) calculation method was used to determine the H---OH TS, where the TS is an intermediate configuration that the potential energy has a maximum value (Supplementary Figs. 56 and 57). Both MoO_2@Mo_2C and Al_P-MoO_2@Mo_2C models show more negative adsorption energies (−0.63 eV and −0.55 eV) of water molecules than that of bare Mo_2C (−0.38 eV) (Fig. 6d), implying that the oxide-termination catalyst surface is more beneficial for the initial adsorption and subsequent cleavage of water molecules relative to bare metal-carbide counterpart[57]. As expected, the calculated energy barriers (ΔG_{H2O}) for water dissociation are 0.03 and 0.09 eV on MoO_2@Mo_2C and Al_P-MoO_2@Mo_2C model, respectively, both are lower than that of bare Mo_2C (0.66 eV) (Fig. 6d). Meanwhile, the calculation detail demonstrates that the OH^- by-products from water dissociation are preferentially adsorbed on the Al_P sites, while the bridging oxygen sites between Mo and Al hetero-nuclear atoms are responsible for the adsorption of desired H* intermediates, confirming the pivotal role of Al_P sites in Al_P-MoO_2@Mo_2C composite system for alkaline HER process. The hydrogen adsorption free energy (ΔG_H) serves as a good descriptor to evaluate the deprotonation kinetics of Al_P-H*x*MoO*y* intermediates, where a moderate ΔG_H value in close to thermoneutral value (0) is usually predicted to be a notable HER catalyst. Although the oxide terminations on carbide structures are effective for breaking the H-OH bond, they are generally inefficient for converting the resultant H* intermediates to H_2 molecules, as determined by the more negative ΔG_H value on MoO_2@Mo_2C catalyst surface relative to bare Mo_2C model. Encouragingly, the Al-tailored MoO_2 termination displays a further optimized deprotonation kinetics with the value of ΔG_H as low as −0.17 eV (Fig. 6e). Interestingly, we observe that the deprotonation activities of Al_P-MoO_2@Mo_2C model can be further optimized by the increased amounts of neighboring hydrogen atoms (Fig. 6f, g, Supplementary data 7–9), implying that the accumulation of protons tailoring the local acid-like catalytic environment can further accelerate deprotonation kinetics, thereby boosting the hydrogen production.

Discussion

In summary, a deliberately customized molybdenum-carbide model-catalyst system is introduced to validate the possibility of termination-acidity tailoring strategy for improved alkaline HER process. Our practical Al_P-MoO_2@Mo_2C composite catalyst with enhanced alkaline-leaching resistance and surface acidity is synthesized by simple hydrothermal and carbonization methods. The well-designed Al_P-MoO_2@Mo_2C composite catalyst shows notbale HER activities, featuring a near-zero onset-potential, a low overpotential (40 mV) at 10 mA/cm^2, and a small Tafel slope (45 mV/dec) in alkaline electrolyte. Moreover, continuous alkaline hydrogen evolution catalyzed by the Al_P-MoO_2@Mo_2C composite catalyst is maintained over 200 h. The impressive activity and stability performances demonstrate that the theory-predicted Pt-like HER performance of metal carbides can indeed be achieved through a feasible termination-acidity tailoring engineering with Al_P atoms. Our work paves an interesting and valuable route for the rational termination tailoring of transition metal carbides towards highly efficient and stable HER process in alkaline electrolyte. Benefiting from our findings, this feasible termination-acidity tailoring strategy holds great promising for extension to explore other forms of low-cost but highly-active catalysts, with the aim of replacing benchmark Pt catalyst in high-pH catalytic hydrogen production and beyond.

Methods

Chemicals

Molybdenum pentachloride ($MoCl_5$ 99%, Aladdin, USA), polyvinylpyrrolidone (PVP, Macklin, China), sodium aluminate ($NaAlO_2$ 99%, Sinopharm Chemical Reagent Co. Ltd, China), polyethylene oxide-*co*-polypropylene oxide-*co*-polyethylene oxide (P_{123} 98%, Adamas Reagent, China), dopamine hydrochloride (DA 98%, Aladdin, USA), 2-amino-2-hydroxymethyl-propane-1,3-diol (Tris 98%, Aladdin, USA) and potassium hydroxide (KOH, 99.999%, Aladdin, USA).

Preparation of Al-MoO_x

In a typical procedure, a mixture of $MoCl_5$ (250 mg), PVP (20 mg), and $NaAlO_2$ (40 mg) compounds was dissolved in absolute ethanol (50 mL) for the formation of homogeneously green solution after stirring for 30 min. Afterwards, the obtained solution was transferred into a 100 mL Teflon-lined autoclave and heated at 180 °C for 12 h. The resultant black Al-MoO_x product was collected after purification and centrifugation. For comparison, MoO_x counterpart was also prepared using the same method without the addition of Al source.

Preparation of DA-Al-MoO_x

The Al-MoO*x* powders were immersed into a mixture solution (100 mL) of DA (80 mg), P_{123} (40 mg), and Tris (20 mg) with continuously stirring for 24 h, then black organic modified Al-MoO_x precursors (DA-Al-MoO_x) were collected after treatments by purification and centrifugation. For comparison, organic modified MoO_x precursors and bare organic materials were also obtained in accordance with the same method.

Preparation of Al_P-MoO_2@Mo_2C

The desired Al_P-MoO_2@Mo_2C was obtained by pyrolyzing the DA-Al-MoO_x precursors at 720 °C for 2 h under an Ar atmosphere. MoO_2@Mo_2C and bare C counterparts were also obtained under the identical conditions.

Preparation of Al-MoO_2@Mo_2C model catalyst

The commercial Mo plate was pretreated by Ar etching and vacuum annealing for the preparation of flatten surface. Al tailored Mo_2C film was prepared by in situ carbonization of Al^{3+} adsorbed pretreated Mo plate at 873 K under 0.3 mbar C_2H_4 atmosphere. The as-obtained metal-carbide film was then oxidized at 573 K under 0.3 mbar O_2 atmosphere, and the desired Al-MoO_2@Mo_2C model catalyst could be obtained. The referenced Mo_2C and MoO_2@Mo_2C films also could be collected based on above methods without the addition of Al source. All composition identifications of Mo_2C and MoO_2 materials are in accordance with the XPS measurements.

Characterization

The XRD pattern was recorded on a Bruker AXS D8 Advance X-ray diffractometer with a Cu Ka radiation target (40 V, 40 A). High-resolution STEM images and the corresponding STEM-EDS elemental maps were measured on an FEI Titan Themis Z 3.1 equipped with a SCOR spherical aberration corrector and a monochromator. The probe convergence angle was 80, and camera length was 115 mm in the STEM mode. X-ray photoelectron spectra (XPS) were collected using ESCALAB 250Xi XPS instrument with Al Kα X-rays as the excitation source and with the gun operated at 15 kV and 10 mA. The contact angle and electrical conductivity tests are performed on Biolin Scientific Attension Theta Flex and physical property measurement system (PPMS, Dyna cool 9T), respectively. BET surface-area test is performed on micromeritics (TriStar II Plus Version 3.03). O K-edge NEXAFS spectra was performed at the Catalysis and Surface Science End-station at the BL11U beamline in the National Synchrotron Radiation Laboratory (NSRL) in Hefei, China. Mo K-edge XAS including XANES and EXAFS profiles were collected at BL11B station at the Shanghai Synchrotron Radiation Facility (SSRF).

Preparation of STEM samples by FIB technique

The cross-sectional samples of fresh and post Al_P-MoO_2@Mo_2C materials were prepared by FIB technique using a lift-out method in accordance with previous report[58]. First, the micro-size sphere powders were dispersed in the mixture of water and ethanol by sonication, then the homogeneously distributed solution was dropped onto the clean Si layer with naturally drying for next operation. Second, the suitable cutting sample can be determined by the corresponding SEM image, then carbon and Pt layers were deposited onto the desired micro-size sphere sample, they can protect the desired cross-sectional region by providing mechanical stability during milling, thus the as-obtained STEM sample is composed of upper carbon and Pt depositions, middle cross-sectional sample, and underlying Si layer. Finally, the cross-sectional sample was transferred to an Omniprobe copper half grid, in order to satisfy the characterization requirement of STEM technique, further Pt deposition was used to weld the slice sample onto the grid for a safe separation from the nanomanipulator by FIB milling, besides, Ga^+ ions (at 5 and 2 kV) were used to remove side damage for a final gentle polish for STEM characterization.

Comprehensive spectroscopy characterizations

TOF-SIMS, NMR, Py-IR characterizations were performed to analyze the surface chemistry of the fresh and post catalysts in accordance with previous reports[59,60]. TOF-SIMS 5-100 instrument (ION-TOF GmbH) with a 30-keV Bi^{3+} as analysis beam was used to conduct the negative and positive TOF-SIMS measurements, where the beam current, raster size, and incident angles are set to be 0.7 pA, 50 × 50 μm^2, and 45°, respectively. ^{1}H and ^{27}Al solid-state NMR characterizations were performed on Bruker AVANCE NEO 400 MHz Wide Bore spectrometer and 400 WB spectrometer equipped with a 4 mm standard bore CP MAS probehead (Bruker BioSpin AG, Fällanden, Switzerland), respectively. For ^{1}H NMR characterization, which is operated at a magnetic field of 9.40T using a tetramethyl silane (TMS) as the chemical shift reference. In detail, the as-obtained ^{1}H NMR data were collected at a spinning rate of 15 kHz with a π/2 pulse width of 3.5 μs, and the s recycle of 5 s. The reference of ^{27}Al NMR characterization is $[Al(H_2O)_6]^{3+}$ with standard d value of 0.00. The X channel of ^{27}Al NMR characterization was set to be 104.27 MHz, and the pulse sequence should be changed into one pulse (0.9 μs, π/12) under a magnetic field

of 9.39 T at 297 K. The well-prepared powder samples were packed in the ZrO_2 rotor closed with Kel-F cap and spun at 12 kHz rate. The ^{27}Al NMR data for each sample was recorded by a total of 100 scans with 2 s recycle delay. A Nicolet 380 FT-IR instrument (Thermo Co., USA) was used to perform the Py-IR measurements. First, the pretreated temperature and time for all catalyst samples were set to be 353 K and 2 h under a vacuum environment, meanwhile, the background spectra was collected in the wavenumber range of 1700-1400 cm^{-1} prior to pyridine molecule adsorption. Second, the pyridine molecules were injected for a adsorption equilibrium state on sample surface. Finally, the physically adsorbed pyridine molecules were fully removed by retreating the sample at 353 K for 4 h under a vacuum condition, and the desired Py-IR data were recorded at 50 and 150 °C, respectively.

Evaluation of HER performance

All electrochemical measurements were performed on a CHI760E electrochemical workstation (Shanghai Chenhua Instrument Co., Ltd, China) by a standard three-electrode setup (electrochemical cell: C002, Tianjin Aida Hengsheng Technology Development Co., Ltd, China) at room temperature, The working, reference, and counter electrodes are glassy carbon electrode (CHI104, Shanghai Chenhua Instrument Co., Ltd, China), Ag/AgCl electrode (CHI111, Shanghai Chenhua Instrument Co., Ltd, China), and carbon rod (C306, Tianjin Aida Hengsheng Technology Development Co., Ltd, China), respectively. The electrolyte used is an Ar-saturated 1 M KOH aqueous solution (pH = 14 ± 0.1), which is freshly prepared prior to electrochemical test. Detailed preparation of working electrode is described below: first, Al_P-MoO_2@Mo_2C (10 mg) powder was dispersed into a mixture solution consisting of ethanol (870 μL), water (100 μL), and Nafion (30 μL); second, by the assistance of sonication for more than 30 min, a homogeneous catalyst ink was formed; finally, the catalyst film was prepared by dropping the catalyst ink (20 μL) onto a polished glassy carbon electrode (diameter: 3 mm) with loading mass of 2.83 mg/cm^2. For comparison, all working electrodes for catalyst counterparts were prepared using the same method, while the working electrode supporting commercial Pt/C catalyst was prepared by keeping the same loading to that of desired Al_P-MoO_2@Mo_2C catalyst. In addition, all potentials in this work were collected against the Ag/AgCl electrode and calibrated with respect to a RHE in accordance with our potential calibration test in Supplementary Fig. 20, and the calibration equation is shown below.

$$E_{RHE} = E_{Ag/AgCl} + 1.02V \quad (1)$$

EIS measurements were conducted by applying an AC voltage with an amplitude of 5 mV over a frequency range from 100 kHz to 0.01 Hz. The ECSA value can be calculated by normalizing the double layer capacitance (C_{dl}) of the electrode with specific capacitance ($C_{dl\mathrm{ref}}$) of a flat surface (ECSA = $C_{dl}/C_{dl\mathrm{ref}}$). Similar to previous work[41,61,62], the value of $C_{dl\mathrm{ref}}$ is assumed to be of 40 μF/cm^2 in our work. All data were collected without iR correction unless explicitly specified.

DFT calculations

The plane-wave-based DFT method, as implemented in the Vienna Ab Initio Simulation Package (VASP), along with periodic slab models, was utilized for all computations in this study. The simulations were carried out using projector augmented wave potentials with the Perdew–Burke–Ernzerhof exchange-correlation functional, and set at an energy cut-off of 450 eV. The long-range van der Waals (vdW) interactions were accounted for using the DFT-D3 approach. The VASPKIT tool was employed to generate *k*-point meshes for geometry optimization and self-consistent field energy calculations, with a grid separation of 0.04 $Å^{-1}$. The convergence criteria for total energy and interaction force were set at 10^{-6} eV and 10^{-2} eV/Å, respectively.

On the basis of the high-resolution lattice fringes by TEM characterization, the DFT models of Mo_2C and MoO_2 materials were established by cleaving the (001) plane of bulk Mo_2C and (010) bulk MoO_2, respectively. In experiments, both the XRD pattern and corresponding high-resolution STEM images have confirmed the existence of (100), (002), and (101) facets of hexagonal Mo_2C phase, and we have also prepared the crystallized MoO_2 (weak crystallization) termination on Mo_2C carbide structure with typical (011) and (020) facets. In theory, both $(001)_{Mo2C}$ and $(010)_{MoO2}$ facets have the similar hexagonal atom arrangements ($(001)_{Mo2C}$ and $(010)_{MoO2}$ facets are parallel to the observed $(002)_{Mo2C}$ and $(020)_{MoO2}$ ones, respectively), and the lattice mismatch of $(001)_{Mo2C}$ and $(010)_{MoO2}$ facets is calculated to be of 1.37%, which is smaller than that (3.31%) of $(001)_{Mo2C}$ and $(011)_{MoO2}$ counterpart. Therefore, $(001)_{Mo2C}$ and $(010)_{MoO2}$ (which was modified by randomly remove some oxygen atoms) facets were selected to establish the DFT model. A vacuum region of 15 Å was set along the *z* direction to avoid the interaction between periodic images. The optimized in-plane lattice parameters were 5.78 Å and 5.79 Å for Mo_2C (001) plane, and 5.51 Å and 5.57 Å for MoO_2 (010) plane. The MoO_2/Mo_2C interface was constructed by placing the MoO_2 slab on the Mo_2C substrate, and the interface in-plane lattice parameters were set to be the average value of those of Mo_2C (001) and MoO_2 (010) planes, guaranteeing the <3% lattice mismatch. A 2 × 2 supercell was then built to server as the HER reaction substrate. The doping of Al was modeled by substitute the Mo atoms at MoO_2 surface with Al atoms.

For the energy-barrier calculation of water dissociation, NEB method was used to determine the transition state, where the free energy of adsorbed H (ΔG_H) on surface is calculated in accordance with the following Eq. (2):

$$\Delta G_H = \Delta E_H + \Delta E_{ZPE} - T\Delta S \quad (2)$$

The above-mentioned parameters of ΔE_H, ΔE_{ZPE}, ΔS, and T are hydrogen adsorption energy, zero point energy difference, entropy difference, and system temperature (298.15 K), respectively. In addition, both zero point energy difference and entropy difference are derived from the comparison of the adsorbed state and gas phase for adsorbate.

Data availability

Source Data file has been deposited in Figshare under accession code DOI link. https://doi.org/10.6084/m9.figshare.26510089. Where[62] is the numbered reference of the data in the repository in the reference list.

References

1. Xie, H. P. et al. A membrane-based seawater electrolyser for hydrogen generation. *Nature* **612**, 673–678 (2022).
2. Yu, Z. Y. et al. Clean and affordable hydrogen fuel from alkaline water splitting: past, recent progress, and future prospects. *Adv. Mater.* **33**, 2007100 (2021).
3. Luo, Y. T. et al. Recent advances in design of electrocatalysts for high-current-density water splitting. *Adv. Mater.* **34**, 2108133 (2022).
4. Wu, T. et al. Engineering metallic heterostructure based on Ni_3N and 2M-MoS_2 for alkaline water electrolysis with industry-compatible current density and stability. *Adv. Mater.* **34**, 2108505 (2022).
5. Subbaraman, R. et al. Enhancing hydrogen evolution activity in water splitting by tailoring Li^+-$Ni(OH)_2$-Pt interfaces. *Science* **334**, 1256–1260 (2011).
6. Dinh, C. T. et al. Multi-site electrocatalysts for hydrogen evolution in neutral media by destabilization of water molecules. *Nat. Energy* **4**, 107–114 (2019).

7. Chen, J. G. G. Carbide and nitride overlayers on early transition metal surfaces: preparation, characterization, and reactivities. *Chem. Rev.* **96**, 1477–1498 (1996).
8. Mahmood, J. et al. An efficient and pH-universal ruthenium-based catalyst for the hydrogen evolution reaction. *Nat. Nanotechnol.* **12**, 441–446 (2017).
9. Zhang, Q. et al. Trends and descriptors of metal-modified transition metal carbides for hydrogen evolution in alkaline electrolyte. *ACS Catal.* **9**, 2415–2422 (2019).
10. Gao, Q. S. et al. Noble-metal-free electrocatalysts: structural design and electronic modulation of transition-metal-carbide electrocatalysts toward efficient hydrogen evolution. *Adv. Mater.* **31**, 1802880 (2019).
11. Hwu, H. H. et al. Surface chemistry of transition metal carbides. *Chem. Rev.* **105**, 185–212 (2005).
12. Anasori, B. et al. 2D metal carbides and nitrides (MXenes) for energy storage. *Nat. Rev. Mater.* **2**, 16098 (2017).
13. Zhang, X. et al. A novel Ni-MoC_xO_y interfacial catalyst for syngas production via the chemical looping dry reforming of methane. *Chem* **9**, 102–116 (2023).
14. Sudarsanam, P. et al. Supported MoO_x and WO_x solid acids for biomass valorization: interplay of coordination chemistry, acidity, and catalysis. *ACS Catal.* **11**, 13603–13648 (2021).
15. Jiang, X. L. et al. The heterostructure of Ru_2P/WO_3/NPC synergistically promotes H_2O dissociation for improved hydrogen evolution. *Angew. Chem. Int. Ed.* **60**, 4110–4116 (2021).
16. Smith, R. L. et al. The protonation of MoO_3 during the partial oxidation of alcohols. *J. Catal.* **173**, 219–228 (1998).
17. Fu, J. Y. et al. Modulating the dynamics of Brønsted acid sites on $PtWO_x$ inverse catalyst. *Nat. Catal.* **5**, 144–153 (2022).
18. Chen, J. D. et al. Reversible hydrogen spillover in Ru-WO_{3-x} enhances hydrogen evolution activity in neutral pH water splitting. *Nat. Commun.* **13**, 5382 (2022).
19. He, L. Q. et al. Molybdenum carbide-oxide heterostructures: in situ surface reconfiguration toward efficient electrocatalytic hydrogen evolution. *Angew. Chem. Int. Ed.* **59**, 3544–3548 (2020).
20. Huang, X. et al. Unraveling the oxide layer on Mo_2C as the active center for hydrogen evolution reaction. *J. Catal.* **389**, 461–467 (2020).
21. Hunt, S. T. et al. Engineering non-sintered, metal-terminated tungsten carbide nanoparticles for catalysis. *Angew. Chem. Int. Ed.* **53**, 3544–3548 (2014).
22. Chen, Y. S. et al. Tantalum oxide-supported metal oxide (Re_2O_7, CrO_3, MoO_3, WO_3, V_2O_5, and Nb_2O_5) catalysts: synthesis, Raman characterization and chemically probed by methanol oxidation. *J. Catal.* **217**, 468–477 (2003).
23. Ko, Y. J. et al. Tungsten carbide nanowalls as electrocatalyst for hydrogen evolution reaction: new approach to durability issue. *Appl. Catal. B Environ.* **203**, 684–691 (2017).
24. Chu, S. Y. et al. Pinning effect enhanced structural stability toward a zero-strain layered cathode for sodium-ion batteries. *Angew. Chem. Int. Ed.* **60**, 13366–13371 (2021).
25. Yoon, G. H. et al. Enabling stable and nonhysteretic oxygen redox capacity in Li-excess Na layered oxides. *Adv. Energy Mater.* **12**, 2103384 (2022).
26. Zhang, S. L. et al. Al^{3+} intercalation/de-intercalation-enabled dual-band electrochromic smart windows with a high optical modulation, quick response and long cycle life. *Energy Environ. Sci.* **11**, 2884–2892 (2018).
27. Wu, C. et al. High-performance aqueous Zn^{2+}/Al^{3+} electrochromic batteries based on niobium tungsten oxides. *Adv. Funct. Mater.* **33**, 2214886 (2023).
28. Xu, J. et al. Metal active sites and their catalytic functions in zeolites: insights from solid-state NMR spectroscopy. *Acc. Chem. Res.* **52**, 2179–2189 (2019).
29. Steen, E. V. et al. A DFT-study on the acidity of Mo-O-Al-clusters. *J. Mol. Catal. A Chem.* **266**, 254–259 (2007).
30. Liu, D. S. et al. Manipulating OH-mediated anode-cathode cross-communication toward long-life aqueous zinc-vanadium batteries. *Angew. Chem. Int. Ed.* **62**, e202215385 (2023).
31. Faisal, F. et al. Electrifying model catalysts for understanding electrocatalytic reactions in liquid electrolytes. *Nat. Mater.* **17**, 592–598 (2018).
32. Over, H. Fundamental studies of planar single-crystalline oxide model electrodes (RuO_2, IrO_2) for acidic water splitting. *ACS Catal.* **11**, 8848–8871 (2021).
33. Chen, Z. G. et al. Thermal migration towards constructing W-W dual-sites for boosted alkaline hydrogen evolution reaction. *Nat. Commun.* **13**, 763 (2022).
34. Chen, L. et al. Mo-based ultrasmall nanoparticles on hierarchical carbon nanosheets for superior lithium ion storage and hydrogen generation catalysis. *Adv. Energy Mater.* **7**, 1602782 (2017).
35. Sun, Y. M. et al. Self-assembled hierarchical MoO_2/graphene nanoarchitectures and their application as a high-performance anode material for lithium-ion batteries. *ACS Nano* **5**, 7100–7107 (2011).
36. Liu, X. et al. Comprehensive understandings into complete reconstruction of precatalysts: synthesis, applications, and characterizations. *Adv. Mater.* **33**, 2007344 (2021).
37. Wu, S. W. et al. Single Cu-N_4 sites enable atomic Fe clusters with high-performance oxygen reduction reactions. *Energy Environ. Sci.* **16**, 3576–3586 (2023).
38. Zhu, Y. M. et al. Facilitating alkaline hydrogen evolution reaction on the hetero-interfaced Ru/RuO_2 through Pt single atoms doping. *Nat. Commun.* **15**, 1447 (2024).
39. Xu, W. W. et al. Ag nanoparticle-induced surface chloride immobilization strategy enables stable seawater electrolysis. *Adv. Mater.* **36**, 2306062 (2024).
40. Li, G. W. et al. In situ modification of a delafossite-type $PdCoO_2$ bulk single crystal for reversible hydrogen sorption and fast hydrogen evolution. *ACS Energy Lett.* **4**, 2185–2191 (2019).
41. Zhang, C. et al. Sub-1.1 nm ultrathin porous CoP nanosheets with dominant reactive {200} facets: a high mass activity and efficient electrocatalyst for the hydrogen evolution reaction. *Chem. Sci.* **8**, 2769–2775 (2017).
42. Fang, Z. W. et al. Dual tuning of Ni-CoA (A = P, Se, O) nanosheets by anion substitution and holey engineering for efficient hydrogen evolution. *J. Am. Chem. Soc.* **140**, 5241–5247 (2018).
43. Zhou, Y. N. et al. Tuning charge–discharge induced unit cell breathing in layer-structured cathode materials for lithium-ion batteries. *Nat. Commun.* **5**, 5381 (2014).
44. Purans, J. et al. Study of the electronic structure of rhenium and tungsten oxides on the O K-edge. *Ionics* **4**, 101–105 (1998).
45. Wu, J. F. et al. Mechanistic insight into the formation of acetic acid from the direct conversion of methane and carbon dioxide on zinc-modified H-ZSM-5 zeolite. *J. Am. Chem. Soc.* **135**, 13567–13573 (2013).
46. Qi, G. D. et al. Synergic effect of active sites in zinc-modified ZSM-5 zeolites as revealed by high-field solid-state NMR spectroscopy. *Angew. Chem. Int. Ed.* **55**, 15826–15830 (2016).
47. Chen, J. L. et al. Regulation of framework aluminum siting and acid distribution in H-MCM-22 by boron incorporation and its effect on the catalytic performance in methanol to hydrocarbons. *ACS Catal.* **6**, 2299–2313 (2016).
48. Kato, Y. et al. Quantification of aluminium coordinations in alumina and silica-alumina by Al K-edge XANES. *Phys. Chem. Chem. Phys.* **3**, 1925–1929 (2001).
49. Kwak, J. H. et al. Coordinatively unsaturated Al^{3+} centers as binding sites for active catalyst phases of platinum on g-Al_2O_3. *Science* **325**, 1670–1673 (2009).

50. Duan, H. M. et al. Penta-coordinated Al^{3+} stabilized active Pd structures on Al_2O_3 coated palladium catalysts for methane combustion. *Angew. Chem. Int. Ed.* **58**, 12043–12048 (2019).
51. Xue, X. Y. et al. High-pressure δ-$Al(OH)_3$ and δ-AlOOH phases and isostructural hydroxides/oxyhydroxides: new structural insights from high-resolution ^1H and ^{27}Al NMR. *J. Phys. Chem. B* **111**, 13156–13166 (2007).
52. Hill, M. R. et al. Integrated study of the calcination cycle from gibbsite to corundum. *Chem. Mater.* **19**, 2877–2883 (2007).
53. Jing, G. H. et al. Promotional mechanism of tungstation on selective catalytic reduction of NOx by methane over $In/WO_3/ZrO_2$. *Appl. Catal. B Environ.* **91**, 123–134 (2009).
54. Foo, G. S. et al. Role of Lewis and Brønsted acid sites in the dehydration of glycerol over niobia. *ACS Catal.* **4**, 3180–3192 (2014).
55. Choi, C. S. et al. CO_2-promoted electrocatalytic reduction of chlorinated hydrocarbons. *J. Am. Chem. Soc.* **146**, 8486–8491 (2024).
56. Zhang, Q. et al. Solvation effects on DFT predictions of ORR activity on metal surfaces. *Catal. Today* **323**, 35–43 (2019).
57. Song, F. Z. et al. Interfacing nickel nitride and nickel boosts both electrocatalytic hydrogen evolution and oxidation reactions. *Nat. Commun.* **9**, 4532 (2018).
58. Haigh, S. J. et al. Cross-sectional imaging of individual layers and buried interfaces of graphene-based heterostructures and superlattices. *Nat. Mater.* **11**, 764–767 (2012).
59. Chen, Z. et al. Metallic W/WO_2 solid-acid catalyst boosts hydrogen evolution reaction in alkaline electrolyte. *Nat. Commun.* **14**, 5363 (2023).
60. Jiang, Y. J. et al. An advanced ceramifiable organic-inorganic hybrid polysiloxane coating with superior moisture-resistant property. *J. Eur. Ceram. Soc.* **45**, 116924 (2025).
61. Mo, Q. J. et al. Bimetallic $Ni_{2-x}Co_xP$/N-doped carbon nanofibers: solid-solution-alloy engineering toward efficient hydrogen evolution. *Appl. Catal. B Environ.* **244**, 620–627 (2019).
62. Chen, Z. G. et al. Termination-acidity tailoring of molybdenum carbides for alkaline hydrogen evolution reaction. figshare. https://doi.org/10.6084/m9.figshare.26510089 (2024).
63. Momma, K. et al. VESTA3 for three-dimensional visualization of crystal, volumetric and morphology data. *J. Appl. Cryst.* **44**, 1272–1276 (2011).
64. Humphrey, W. et al. VMD-visual molecular dynamics. *J. Mol. Graph.* **14**, 33–38 (1996).

Acknowledgements

Z.C. would like to acknowledge the supports from the National Natural Science Foundation of China (No. 22109171), the Chongqing Talent Program (No. cstc2024ycjh-bgzxm0068), the Science and Technology Research Program of Chongqing Municipal Education Commission (No. KJZD-K202301101), the Natural Science Foundation of Chongqing (No. CSTB2023NSCQ-MSX0315). Y.C. would like to acknowledge the supported from the National Key R&D Program of China (No. 2022YFA1503801, No. 2022YFA1503802), the National Natural Science Foundation of China (No. 22172190), the CAS Project for Young Scientists in Basic Research (No. YSBR-022), and the Young Cross Team Project of CAS (No. JCTD-2021–14). Y.L. would like to acknowledge the support from Natural Science Foundation of Jiangsu Province (No. BK20220290). W.G. would like to acknowledge the support from the Natural Science Foundation of Jiangsu Province (No. BK20231154) and Natural Science Foundation of the Jiangsu Higher Education Institutions of China (No. 22KJA140003). F.M. would like to acknowledge the support from the Cultivation Project of CQUT for Research and Innovation Group (2023TDZ004). The authors are grateful for the technical support of Nano-X from Suzhou Institute of Nano-Tech and Nano-Bionics, Chinese Academy of Sciences (SINANO). We also thank Qing Xu, Jun Hu, Honghe Ding, and Junfa Zhu for their help in Near Edge X-ray Absorption Fine Structure (O *K*-edge NEXAFS) performed at the Catalysis and Surface Science End-station at the BL11U beamline in the National Synchrotron Radiation Laboratory (NSRL) in Hefei, China. We thank Juan Wang for her help in the measurements and analysis of X-ray adsorption spectra (Mo-K edge XAS) characterization at BL11B station in the Shanghai Synchrotron Radiation Facility (SSRF). We thank Fangyuan Zhu from BL07U beamline of Shanghai Synchrotron Radiation Facility (SSRF) for the assistance of data collection for Al K-edge XANES.

Author contributions

Z.C. and Y.C. conceived the project and designed the experiments. Z.C., M.Y., T.L., S.H., and G.Y. performed the synthesis and characterization of catalysts and the electrocatalytic measurements. Z.C., M.Y., and J.W. performed the X-ray adsorption experiment and analyzed the raw data. Z.C., C.Z., and W.G. carried out the DFT calculations. Z.C., Y.L., H.L., and Y.C. performed the experiment of model catalyst and analyzed the data. Z.C., Y.J., C.Z., Z.T., F.M., and Y.C. wrote the paper. All authors discussed the results and commented on the manuscript.

Competing interests

The authors declare no competing interests.

Additional information

Supplementary information The online version contains supplementary material available at https://doi.org/10.1038/s41467-025-55854-6.

Correspondence and requests for materials should be addressed to Yi Cui.

Peer review information *Nature Communications* thanks Huilong Fei, Anantharaj Sengeni and Seung-Jae Shin for their contribution to the peer review of this work. A peer review file is available.